

Band inversion and topology of the bulk electronic structure in $\text{FeSe}_{0.45}\text{Te}_{0.55}$

Himanshu Lohani,¹ Tamaghna Hazra,² Amit Ribak,¹ Yuval Nitzav,¹
Huixia Fu,³ Binghai Yan,³ Mohit Randeria,² and Amit Kanigel¹

¹*Physics Department, Technion-Israel Institute of Technology, Haifa 32000, Israel.*

²*Physics Department, Ohio State University, Columbus, OH 43210, USA*

³*Department of Condensed Matter Physics, Weizmann Institute of Science, Rehovot 7610001, Israel*

(Dated: August 18, 2021)

$\text{FeSe}_{0.45}\text{Te}_{0.55}$ (FeSeTe) has recently emerged as a promising candidate to host topological superconductivity, with a Dirac surface state and signatures of Majorana bound states in vortex cores. However, correlations strongly renormalize the bands compared to electronic structure calculations, and there is no evidence for the expected bulk band inversion. We present here a comprehensive angle resolved photoemission (ARPES) study of FeSeTe as function of photon energies ranging from 15 - 100 eV. We find that although the top of bulk valence band shows essentially no k_z dispersion, its normalized intensity exhibits a periodic variation with k_z . We show, using ARPES selection rules, that the intensity oscillation is a signature of band inversion indicating a change in the parity going from Γ to Z. Thus we provide the first direct evidence for a topologically non-trivial bulk band structure that supports protected surface states.

PACS numbers: 74.25.Jb, 74.70.Dd, 71.20.Be

Iron-based superconductors (FeSCs) have been intensely investigated since their discovery in 2008 [1] as strongly correlated materials that harbor high temperature superconductivity. Recently, interest in this field has increased greatly due to new experiments that suggest that some of these systems may be topological superconductors [2] that harbor Majorana bound states (MBS) in their vortex cores, which could be potentially important for quantum information processing [3].

Wang *et al.* [9] first suggested that $\text{FeSe}_{0.5}\text{Te}_{0.5}$ (FeSeTe) can host topologically protected Dirac surface states, which were recently observed directly using angle resolved photoemission spectroscopy (ARPES) [10]. Soon after, such states were found in other FeSCs [11] and in thin films [7]. In addition, clear zero bias conductance peaks (ZBCP) were observed [8, 9] in the superconducting vortex cores in FeSeTe using scanning tunneling spectroscopy (STS), and identified as the MBS expected in topological superconductors. In fact, the strong correlations in these materials, which leads to surprisingly large Δ/E_F ratios [10, 11], helps in separating the ZBCP from (topologically) trivial vortex core bound states.

Despite these exciting developments, direct evidence for the topological nature of the *bulk* band structure – responsible for the topologically protected surface states and MBS – is lacking. Density functional theory (DFT) calculations [9] for FeSeTe find a p_z band that is highly dispersive along k_z , which mixes with an appropriate linear combination of the $d_{xz,yz}$ bands. As a result, the orbital character and the parity of the band changes as one goes from $\Gamma(0,0,0)$ to $Z(0,0,\pi/c)$. However, no such highly dispersive band is observed in the data, as we shall show below, and – at first sight – there seems to be no evidence for the band inversion expected in a topologically nontrivial bulk band structure.

FeSeTe is known to be the most strongly correlated member of the FeSC family [12, 13], making it difficult to directly compare ARPES measurements with DFT. It offers an exciting opportunity to study the interplay between the topological nature of the band structure and the effect of the strong electronic correlations.

In this letter, we present a systematic ARPES study of FeSeTe for a broad range of incident photon energies (15 to 100 eV) to investigate the k_z -dispersion of the bulk electronic structure. Using symmetry analysis and dipole selection rules, we present clear evidence for the change in the parity eigenvalue going from Γ to Z, in spite of the absence of any highly dispersive band. We also present a tight-binding model, with reasonable values of renormalization parameters relative to DFT and of spin-orbit coupling, which gives insight into ARPES observations. We thus provide compelling evidence for bulk “band inversion”, the hallmark of a topological band structure via the Fu-Kane invariant [14], which leads to a protected Dirac surface state in the energy gap near the Γ point.

We used high quality $\text{Fe}_{1.02}\text{Se}_{0.45}\text{Te}_{0.55}$ single crystals for ARPES measurements. Fig. 1(a,b) shows the geometry of our ARPES experiments. We will focus on near-normal emission with (k_x, k_y) near $(0,0)$, and light incident in the YZ plane in either LV (linear vertical) or LH (linear horizontal) polarizations, as shown. This geometry will be crucial in the analysis of the selection rules later in the paper. Our laboratory axes (X, Y, Z) conform with the literature [10, 11], however, we label orbitals with reference to the crystallographic axes (x, y, z) , irrespective of sample rotations, consistent with Refs. [5, 6, 15].

We show ARPES data along the Γ -M direction using 22 eV LV photons in Fig. 1(c), and its second derivative [18] sharpened image in panel (d). This allows us to see in addition to a dispersive bulk band, which we label as α_1 , an intense state at a binding energy (BE) of around 10 meV, that lies between the top of the α_1 band (BE \simeq 18 meV) and the chemical potential (BE = 0 meV). This state is similar to the linearly dispersive Dirac surface state (SS), recently been reported by Zhang *et al.* [10]. In Fig. 1(e) we show LH polarization data where in addition to the states seen in LV data of panel (c), we also see another dispersive α_2 band.

The ARPES intensity allows a direct mapping of the electronic dispersion for momenta parallel to the sample surface.

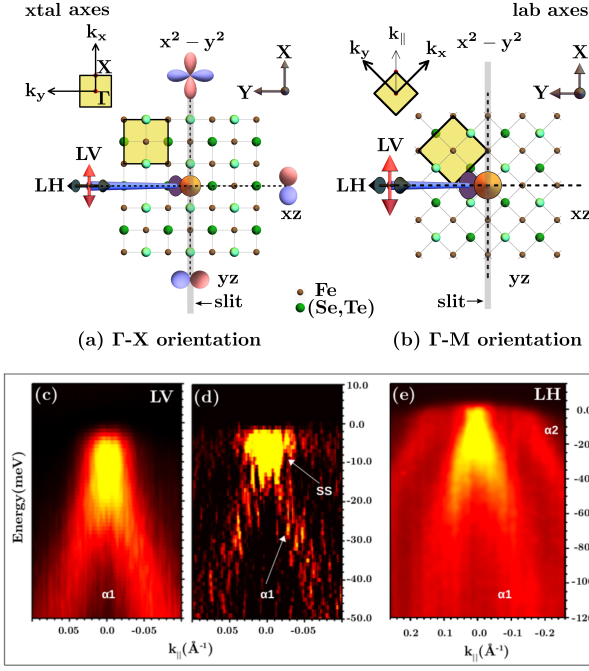


FIG. 1. (a, b) Notation and conventions: s-type ARPES setup with the analyzer slit for emitted electrons in the XZ (vertical) plane, and light incident in the YZ (horizontal) plane in either vertical (LV) or horizontal (LH) polarizations, as shown. The sample is oriented with the analyzer slit along Γ -X (panel a) or Γ -M (panel b). The orbitals are labelled with reference to the crystal coordinate axes (x, y, z) while the laboratory frame is denoted by (X, Y, Z). (c) ARPES image taken along Γ -M direction at $T = 25$ K using 22 eV LV polarized light. (d) Second derivative of the data shown in (c) to emphasize the Dirac surface state. (e) ARPES image for the same sample measured using 22 eV LH polarized light.

This is because only in-plane momentum is conserved in the photoemission process. To map the dispersion along k_z , one needs to scan as a function of the incident photon energy. We use the free-electron final-state approximation to find the correspondence between the photon energy and k_z ; see Suppl. Info. Sec-I for details.

Before turning to the bulk electronic structure (α_1 and α_2 bands), which is our main focus, we first look at that intense state near 10 meV BE. In Fig. 2(a), we show the ARPES intensity map over an extensive photon energy range at a fixed BE = 10 meV, where the x-axis represents k_z (converted from photon energy) and the y-axis represents k_{\parallel} along Γ -X direction. We find intensity at this BE for all k_z values, consistent with a surface state. At these photon energies the k -resolution does not allow us to extract the Dirac-like dispersion of the surface state, we can nevertheless estimate the location of the Dirac point as follows. We make Lorentzian fits to the momentum distribution curves (MDCs) of the ARPES intensity at a fixed BE as a function of k_{\parallel} in Fig. 2(b,c,d), and plot the full width at half maximum (FWHM) of the fits as a function of BE in Fig. 2(e). We estimate the Dirac point to be at 8 meV, the BE at which the MDCs exhibit a smallest FWHM. Crucially, the BE of the Dirac point is independent of the pho-

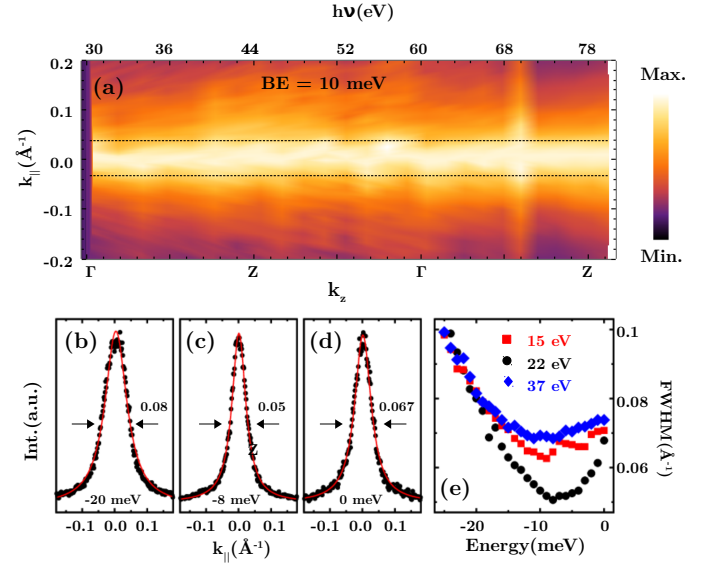


FIG. 2. Surface state: (a) ARPES intensity map at binding energy (BE) of 10 meV, as a function of the in-plane momentum k_{\parallel} along Γ -X (y-axis) and photon energy, which probes different k_z values (x-axis). (b-d) MDCs at 20, 8 and 0 meV BE measured using 22 eV photons with LV polarization. The red lines are Lorentzian fits to the data. (e) Full width at half maximum of Lorentzian fits as a function of BE, for three different photon energies. The BE of the minimum in these curves gives an estimate of the location of the Dirac point.

ton energy, as expected for a surface Dirac state.

We next turn to the band structure of the bulk α_1 and α_2 bands. We will discuss in detail below their orbital content, and the resulting constraints on ARPES selection rules. For now, suffice it to say that both are made up of Fe-derived d_{xz}, d_{yz} orbitals, and α_1 also has an important p_z admixture (See Appendix D).

The in-plane dispersion of α_2 bands, shown in Fig. 1(e), can be fit with a simple (hole-like) parabolic model to determine its top at $(k_x, k_y) = (0, 0)$, even when it lies above the chemical potential; see Appendix C for details. The top of α_1 band is obtained from the $(k_x, k_y) = (0, 0)$ EDC peaks. For α_1 we use LV data (Fig. 1(c)) and for α_2 we use LH data (Fig. 1(e)) and determine the tops of the bands as a function of k_z by changing the incident photon energy.

Our goal is to look for the band inversion predicted by DFT by mapping out the k_z -dispersion, going from $\Gamma(0,0,0)$ to $Z(0,0,\pi/c)$. From Fig. 3(a) we see that the top of the α_2 band, $\epsilon_{\alpha_2}(0,0,k_z)$ shows a periodic variation with k_z with a maximum at Z, a minimum at Γ , and a k_z -bandwidth of about 18 meV. In contrast, the corresponding result for $\epsilon_{\alpha_1}(0,0,k_z)$ in Fig. 3(b) shows essentially no dispersion; see also Ref. [5].

Let us compare these k_z -dispersions with the DFT results shown in Fig. 3(c). The observed α_2 dispersion is at least crudely consistent with upper d_{xz}/d_{yz} band in DFT, if one is willing to renormalize the bandwidth down by a factor of about 5 and make a shift in energy. However, the dispersionless α_1 band seems difficult to reconcile with 100 meV wide d_{xz}/d_{yz} band that crosses a 500 meV wide p_z band in DFT.

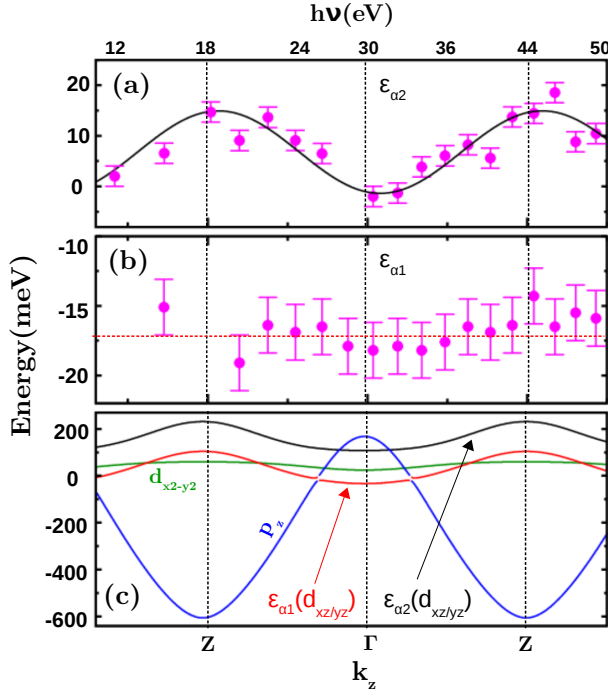


FIG. 3. Bulk band structure: (a) k_z dispersion of the α_2 band extracted from LH polarization ARPES data at different photon energies. (b) k_z dispersion of the α_1 band based on LV polarization ARPES data. (c) DFT band structure along k_z which is very different from the ARPES data; see text for details.

The $d_{x^2-y^2}$ band is not seen in the experiments in the energy-momentum window that we focus on in this work.

To see how the ARPES data can be understood as a renormalized band structure with reasonable parameters, we turn to a tight binding model for the k_z dispersion of FeSeTe. This will also help us to see how selection rules can help address the question of the topological/trivial nature of the band structure. We focus only on $(k_x, k_y) = (0, 0)$ here, although one can use $\mathbf{k} \cdot \mathbf{p}$ perturbation theory to look at k_{\parallel} dispersion; see Appendix D.

We write a minimal model involving p_z , d_{xz} and d_{yz} bands motivated by DFT. The most general Hamiltonian, which includes up to nearest-neighbor hopping, is $H = \sum_{\mathbf{k}} \Psi_{\mathbf{k}}^\dagger h_{\mathbf{k}} \Psi_{\mathbf{k}}$ with the annihilation operator $\Psi_{\mathbf{k}} = (c_{p_z}, c_{d_{yz}}, c_{d_{xz}})^T$ and the Hermitian matrix

$$h_{\mathbf{k}} = \begin{pmatrix} \epsilon_p^0 + 2t_{zp} \cos k_z & -2\lambda_3 \sigma_x \sin k_z & 2\lambda_3 \sigma_y \sin k_z \\ \cdot & \epsilon_d^0 + 2t_{zd} \cos k_z & i\sigma_z (\lambda_1 + 2\lambda_2 \cos k_z) \\ \cdot & \cdot & \epsilon_d^0 + 2t_{zd} \cos k_z \end{pmatrix} \quad (1)$$

where the c-axis lattice spacing $c = 1$. The off-diagonal terms arise from spin-orbit coupling (SOC) and their form is constrained by symmetry. For instance, to obtain the p-d mixing terms, we note that the even-parity band must transform like p_z under the C_{4v} transformations that leave $\mathbf{k} = (0, 0, k_z)$ invariant. Only then can the two bands hybridize along ΓZ . One can check that the operator $\sigma_x c_{i,d_{yz}}^\dagger - \sigma_y c_{i,d_{xz}}^\dagger$ transforms

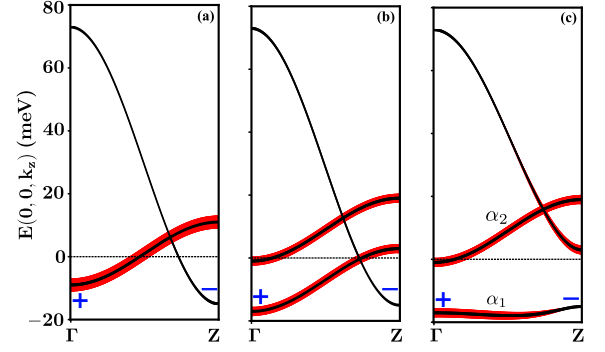


FIG. 4. (a) Bulk dispersion along ΓZ with all spin-orbit coupling (SOC) turned off (left), with splitting between d orbitals turned on (middle) and with SOC between p and d orbitals turned on (right). The parity of the bands at the time-reversal invariant momenta Γ and Z is indicated by the blue symbols. The flat α_1 band undergoes band inversion. The size of the markers schematically represents the weight of the d_{xz} orbital, which is visible in LV polarization; see text.

according to the trivial representation of C_{4v} , just like the p_z orbital. The additional form factor of $\sin k_z$ is required by inversion symmetry. See Appendix D for details.

Guided by the experimentally observed dispersion in Fig. 3 (a,b), we choose parameter values (all in meV) $\epsilon_p^0 = 29$, $\epsilon_d^0 = 1$, $t_{zp} = 22$, $t_{zd} = -5$, and λ_i 's described below. The resulting band structure is shown in Fig. 4. In Fig. 4(a), where all λ_i 's are set to zero, we see the dispersive p_z -band and the degenerate d_{xz} and d_{yz} bands. The ratio $|t_{zp}/t_{zd}|$ is chosen to be similar to the DFT value, although both hoppings are suppressed by interactions. In Fig. 4(b), we see the d-d splitting arising from $\lambda_1 = 8$ meV, keeping $\lambda_2 = 0$ for simplicity. At this stage, the lower band eigenfunctions are equal admixtures of d_{xz} and d_{yz} orbitals, i.e. $(|d_{xz}\rangle + i|d_{yz}\rangle) |\downarrow\rangle$ and its time-reversed partner.

Finally, in Fig. 4(c) we turn on p-d mixing $\lambda_3 = 8$ meV and obtain an essentially flat α_1 band, together with an α_2 band that retains its dispersion. Thus we can understand the ARPES observations with reasonable parameter values for band renormalizations and SOC. In Appendix E, we show that these results are obtained for a range of parameters and not fine-tuned.

We also see from Fig. 4(c) that the orbital character of the α_1 band changes from d -like to p -like going from Γ to Z with a corresponding change in parity eigenvalue. This band inversion is responsible for the non-trivial Fu-Kane invariant [14] of the topological band structure in inversion-symmetric FeSeTe.

We next show how this impacts ARPES selection rules [13] by looking at the matrix element $\langle \psi_f | \mathbf{A} \cdot \mathbf{p} | \psi_i \rangle$ in the experimental geometry of Fig. 1(a). For normally emitted photoelectrons, only those final states $|\psi_f\rangle$ that are even under reflections in the YZ-plane (π_X) and in the XZ-plane (π_Y) have non-zero amplitude at the detector. For LV polarization, $\mathbf{A} \parallel \hat{\mathbf{X}}$ (Fig. 1(a)) which is odd under π_X and even under π_Y . This implies only initial states $|\psi_i\rangle$ which are odd under π_X and even under π_Y should be visible. Thus, when lab (XY) and crystal (xy) axes are aligned, as in Fig. 1(a), only d_{xz} initial states

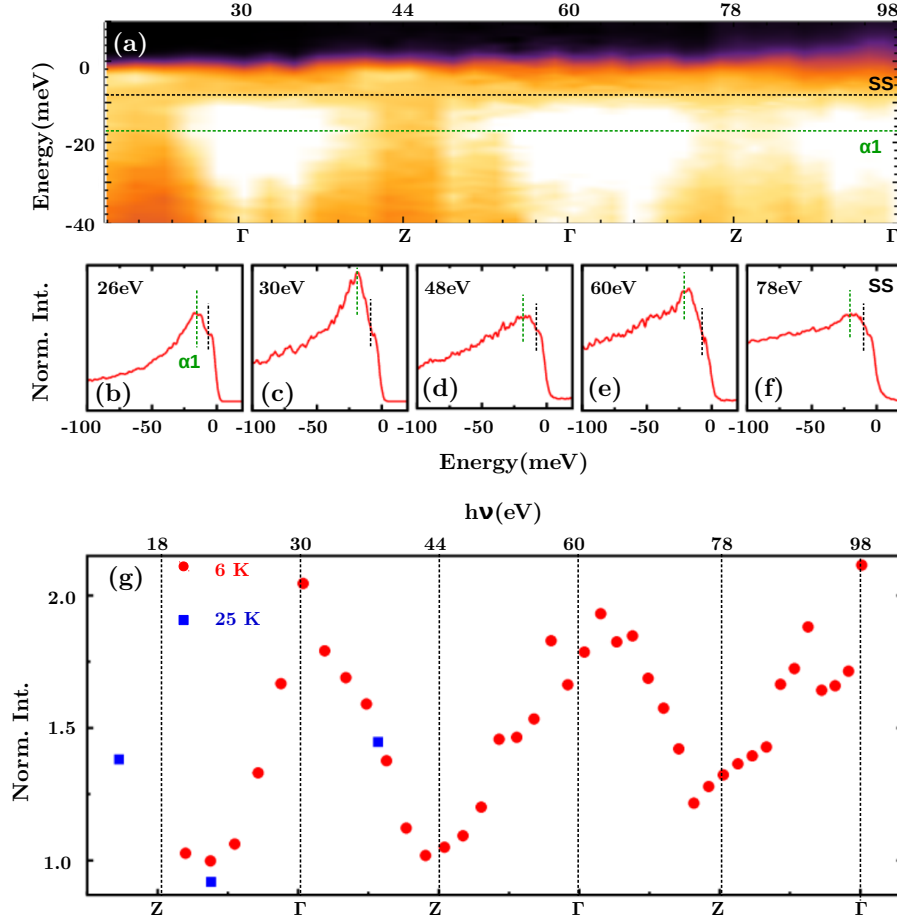


FIG. 5. Periodic variation of orbital character of α_1 as a signature of band inversion: (a): Band dispersion along the k_z direction which is prepared from the EDCs at $k_{\parallel} = 0$ at different photon energies (20 to 98 eV) using LV polarized light. Here, EDCs at different photon energies are normalized to have the same spectral weight at the SS position (BE = 8 meV). Green and black dotted lines mark the BE of the α_1 and SS respectively. In (b,c,d,e and f) the normalized EDC for the selected photon energies 26, 30, 48, 60 and 78 eV are displayed, where vertical dashed green and black lines indicate the position of the α_1 and SS respectively. (g) The normalized ARPES intensity of the α_1 band plotted as a function of incident photon energy, or equivalently k_z . The observed periodic variation of the normalized α_1 intensity as a function of k_z with a maximum at Γ and a minimum at Z is consistent with the band inversion characteristic of a topological electronic structure.

contribute to ARPES with LV polarization. (see Appendix B for a detailed review of selection rules in other cases.)

In Fig. 4(c), we schematically indicate by the width of the red line the weight of the d_{xz} orbital. We thus expect the ARPES intensity in LV polarization to exhibit strong variation with photon energy, as k_z varies from Γ , where you expect a strong contribution from the even parity d_{xz} state, to Z, where the intensity from d_{xz} should be suppressed.

To test this experimentally, we need to normalize the ARPES intensity before we can compare the signals at two different photon energies. A convenient normalization is to use the k_z -independent surface state (SS) at BE = 8 meV discussed above (see Fig. 2). In Fig. 5(g), we plot the variation with photon energy of the intensity at the top of the α_1 band in LV polarization, normalized at each photon energy by the intensity at BE = 8 meV. We thus obtain the main result of our paper: a clear periodic variation of the normalized intensity over a range of photon energy spanning almost three Brillouin

zones, with a maximum at Γ and a minimum at Z, fully consistent with the band inversion characteristic of a topologically non-trivial bulk band structure.

We note that this periodic variation in the normalized intensity at the top of α_1 is clearly visible in the EDC of normally emitted photoelectrons shown for a few selected photon energies in Fig. 5(b-f), and in the variation of intensity with photon energy on the x-axis and binding energy on the y-axes in Fig. 5(a).

In conclusion, the electronic structure of FeSeTe poses a unique challenge where one has to deal with both strong correlations and band topology. DFT calculations predict a highly dispersive bulk band structure along k_z which seems to be essential for the band inversion that leads to a topologically protected Dirac surface state. However, the observed bulk band structure is strongly renormalized by correlations and shows essentially no k_z -dispersion, in marked contrast with the DFT predictions, and raises doubts about band inversion. Through

a combination of extensive ARPES data as a function of photon energy and a careful examination of the orbital character of the bulk bands using selection rules, we show that the α_1 band at the Z point is in fact inverted with respect to Γ , despite the lack of k_z -dispersion. Our modeling provides a natural explanation in terms of renormalized band widths that are comparable to the spin-orbit coupling. We thus reveal an unusual situation where an almost flat band undergoes band inversion, characteristic of a topologically non-trivial bulk band structure.

Methods:

Sample preparation - High-quality single crystals of $\text{Fe}_{1.02}\text{Se}_{0.45}\text{Te}_{0.55}$ were grown using the modified Bridgman method. The stoichiometric amounts of high-purity Fe, Se, and Te powders were grinded, mixed, and sealed in a fused silica ampoule. The ampoule was evacuated to a vacuum better than 10^{-5} torr, and the mixture was reacted at 750°C for 72 hours. The resulting sinter was then regrinded and put in a double-wall ampoule that was again evacuated to a vacuum better than 10^{-5} torr.

The ampoule was placed in a two-zone furnace with a gradient of $5^\circ\text{C}/\text{cm}$ and slowly cooled from 1040°C to 600°C at a rate of $2^\circ\text{C}/\text{hour}$, followed by a faster cooldown to 360°C for 24 hours. The resulting boule contained single crystals that could be separated mechanically. To improve the uniformity of the superconducting phase, we annealed the crystals for 48 hours in ampoules that were evacuated and then filled them with 10^{-3} torr of oxygen. Crystallinity of the prepared single crystals confirmed by XRD measurements and elemental composition determined through energy dispersive X-ray (EDX) analysis [10, 11].

ARPES - High-resolution ARPES measurements were performed at the UE112-PGM-2b-1³ beamline at BESSY (Berlin, Germany), at the I05 beamline at Diamond (Didcot, UK) and at the SIS beamline at the SLS, PSI (Villigen, Switzerland) using photon energies between 15 eV and 150 eV. The samples were cleaved in vacuum better than 5×10^{-11} torr at low temperature and measured for not more than 6 hours. The base temperature at BESSY was 1 K and at Diamond was 6 K. The energy resolution was 4 meV in these beamlines. At PSI, the temperature was 25 K and the energy resolution was 10 meV.

DFT - To resolve the band structure of $\text{FeSe}_{0.45}\text{Te}_{0.55}$, density functional theory (DFT) calculations with spin-orbit coupling were performed using the Vienna ab initio simulation package (VASP) with core electrons represented by the projector-augmented-wave (PAW) potential [20]. Generalized-gradient-approximation (GGA) [21] functional was used for the exchange-correlation potential. To treat the alloy, we perform the DFT calculation using the virtual crystal approximation with ordered Se and Te sites in the two-formula cell. Plane waves with a kinetic energy cut-off of 300 eV were used as the basis set. A k-point grid of $20 \times 20 \times 20$ was used for Brillouin zone sampling.

Acknowledgements: M.R. would like to thank A. Chubukov and H. Ding for stimulating discussions. We gratefully acknowledge support from the US-Israel Binational Science Foundation grant 2014077. H.L. is supported in part at Israel Institute of Technology, Technion by a PBC fellowship of the Israel Council for Higher Education. Work at the Technion was supported by the Israeli Science Foundation Grant 320/17. We thank the Helmholtz-Zentrum Berlin for the allocation of synchrotron radiation beamtime. We acknowledge Diamond Light Source for time on Beamline I05 under Proposal SI15822. We acknowledge the Paul Scherrer Institut, Villigen, Switzerland for provision of synchrotron radiation beamtime at beamline SIS of the SLS. The research leading to these results has received funding from the European Union's Horizon 2020 research and innovation programme under grant agreement no 730872, project CALIPSOplus

-
- [1] Hsu, F.C. et al. Superconductivity in the PbO-type structure α -FeSe *PNAS* **105**, 14262-14264 (2008).
 - [2] Qi, X.L. and Zhang, S.C. Topological insulators and superconductors *Rev. Mod. Phys.* **83**, 1057-1110 (2011).
 - [3] Kitaev, A. Y. Fault-tolerant quantum computation by anyons *Annals Phys.* **303**, 2-30 (2003).
 - [4] Wang, Z. et al. Topological nature of the $\text{FeSe}_{0.5}\text{Te}_{0.5}$ superconductor *Phys. Rev. B* **92**, 115119 (2015).
 - [5] Zhang, P. Observation of topological superconductivity on the surface of an iron-based superconductor *Science* **360**, 182-186 (2018).
 - [6] Zhang, P. Multiple topological states in iron-based superconductors *Nat. Phys.* **15**, 41-47 (2019).
 - [7] Peng, X.L. et al. Observation of topological transition in high- T_c superconductor $\text{FeTe}_{1-x}\text{Se}_x/\text{SrTiO}_3(001)$ monolayers *arXiv:1903.05968*
 - [8] Wang, D. et al. Evidence for Majorana bound states in an iron-based superconductor *Science* **362**, 333-335 (2018).
 - [9] Machida, T. et al. Zero-energy vortex bound state in the superconducting topological surface state of $\text{Fe}(\text{Se},\text{Te})$ *arXiv:1812.08995v2*
 - [10] Lubashevsky, Y., Lahoud, E., Chashka, K., Podolsky, D. and Kanigel, A. Shallow pockets and very strong coupling superconductivity in $\text{FeSe}_x\text{Te}_{1-x}$ *Nat. Phys.* **8**, 309 (2012).
 - [11] Rinott, S. et al. Tuning across the BCS-BEC crossover in the multiband superconductor $\text{Fe}_{1+y}\text{Se}_x\text{Te}_{1-x}$: An angle-resolved photoemission study *Sci. Adv.* **3**, e1602372 (2017).
 - [12] Tamai, A. et al. Strong Electron Correlations in the Normal State of the Iron-Based $\text{FeSe}_{0.42}\text{Te}_{0.58}$ Superconductor Observed by Angle-Resolved Photoemission Spectroscopy *Phys. Rev. Lett.* **104**, 097002 (2010).
 - [13] Yin, Z.P., Haule, K. and Kotliar, G. Kinetic frustration and the nature of the magnetic and paramagnetic states in iron pnictides and iron chalcogenides *Nat. Mat.* **10**, 932 (2011).
 - [14] Fu, L. and Kane, C.L. Topological insulators with inversion symmetry *Phys. Rev. B* **76**, 045302 (2007).
 - [15] Chen, F. et al. Electronic structure of $\text{Fe}_{1.04}\text{Te}_{0.66}\text{Se}_{0.34}$ *Phys. Rev. B* **81**, 014526 (2010).
 - [16] Johnson, P. et al. Spin-Orbit Interactions and the Nematicity Observed in the Fe-Based Superconductors. *Phys. Rev. Lett.* **114**, 167001 (2015).
 - [17] Xu, G., Lian, B., Tang, P., Qi, X.-L. and Zhang, S.-C. Topolog-

ical Superconductivity on the Surface of Fe-Based Superconductors. *Phys. Rev. Lett.* **117**, 047001 (2016).

- [18] Zhang, P. et al. A precise method for visualizing dispersive features in image plots *Rev. Sci. Instr.* **82**, 043712 (2011).
- [19] J. Hermanson, Final-state symmetry and polarization effects in angle-resolved photoemission spectroscopy *Sol. Stat. Comm.* **22**, 9 (1977).
- [20] G. Kresse and J. Hafner, Norm-conserving and ultrasoft pseudopotentials for first-row and transition elements *J. Phys.: Condens. Matter* **6**, 8245 (1994).
- [21] J. P. Perdew, K. Burke, and M. Ernzerhof, Generalized gradient approximation made simple, *Phys. Rev. Lett.* **77**, 3865 (1996).

Appendix A: Photon energy to k_z mapping

The relation $k_z = \sqrt{\frac{2m}{\hbar^2}} \sqrt{(h\nu - \phi - E_B) \cos^2 \theta + V_0}$, where ϕ , E_B , θ and V_0 correspond to work function, BE of photoelectron, emission angle of photoelectron with respect to the sample normal and inner potential of the sample respectively[1], allows a conversion between incident photon energy and k_z for a known inner potential.

The constant V_0 is specific to the material and can be determined experimentally from the ARPES data, by identifying the high-symmetry points in the dispersion along k_z of a band.

Fig.6(a) shows FeSeTe band dispersion along the $\Gamma(0,0,0)$ to $Z(0,0,\pi/c)$ direction calculated using DFT. We choose to use the d_{z^2} band, marked in red, for extracting the value of the inner potential. For that purpose we measured the ARPES spectra at normal emission over a large binding energy range for photon energies varying between 80 eV to 150 eV. The measurements were done at 25K in a p-type configuration, where the incident plane of light is parallel to the analyser slit with the sample oriented along the Γ -M direction.

The results, binding energy of d_{z^2} as a function of photon energy, are shown in Fig.6(b). The DFT dispersion of the same band as a function of k_z is shown in Fig.6(c). The best agreement between the experimental and calculated bands is achieved for an inner potential value of 13 eV. The measured bandwidth is in reasonable agreement with the calculation although the band is shifted by about 400 meV.

Appendix B: ARPES Selection Rules

We now review the ARPES selection rules for the s-configuration setup shown schematically in Fig.7(a) by considering the matrix element $\langle \psi_f | \mathbf{A} \cdot \mathbf{p} | \psi_i \rangle$. Detection of the final state requires that its wavefunction $|\psi_f\rangle$ must be invariant under the symmetries that keep the emitted ray (orange arrow) invariant. For normal emission, this includes both π_Y : reflection about the emission plane (XZ), and π_X : reflection about the incident plane (YZ). Away from normal emission, only π_Y keeps the emitted ray invariant. If the polarization vector \mathbf{A} has definite parity under these symmetries, the matrix element is non-zero only for orbitals that have the same parity. Only those bands are visible which have finite weight in these orbitals. The selection rules for different cases are explicitly

TABLE I. List of allowed orbitals at normal emission for LH and LV polarization.

Sample orientation along Γ -X	
Polarization	Allowed Orbital
LH	$d_{yz}, d_{x^2-y^2}, d_{z^2}, p_z$
LV	d_{xz}
Sample orientation along Γ -M	
LH	$(d_{xz}+d_{yz}), d_{xy}, d_{z^2}, p_z$
LV	$(d_{xz}-d_{yz})$

shown in Fig. 7(d). Note that when the sample is rotated as in Fig. 7(c), the orbitals with definite parity under reflection are not d_{xz}, d_{yz} defined with reference to the crystallographic axes [2]. For LH polarization away from normal emission, there are no symmetry-enforced selection rules since the polarization vector does not have definite parity under π_Y .

Appendix C: Estimation of top of α_2 band

Fig.4(a) represents ARPES image of FeSeTe sample along the Γ -M direction which is collected at photon energy 22 eV utilizing photons of LH polarization. MDC line profile at BE = 25 meV extracted from this image is displayed in Fig.4(b). This MDC profile is fitted to Lorentzian function with three peaks to track the band dispersion of the α_2 band as shown in Fig.4(c). This band dispersion is fitted to a parabolic dispersion to estimate the apex of $\alpha_2(\epsilon_{\alpha_2})$ band.

Appendix D: Derivation of model Hamiltonian

The space group of FeSe_{0.45}Te_{0.55} is actually $P4/nmm$ because of the buckled square lattice, with the chalcogen atoms alternately above and below the Fe plane. We use the existence of a one-to-one mapping [16] between the point group D_{4h} and the space group $P4/nmm$ modulo lattice translations, to describe the physics near Γ -Z in terms of the more well-known D_{4h} group.

We use the method of invariants [3] to construct the most general symmetry-allowed Hamiltonian $H = \sum_n c_n I_n$ where I_n are fermionic bilinears of the form

$$I_n = \sum_{\mathbf{k}, i, \mu, \nu, \alpha, \beta} h_{n\mu\nu}^i(\mathbf{k}) c_{\mathbf{k}\mu\alpha}^\dagger \sigma_{\alpha\beta}^i c_{\mathbf{k}\nu\beta} \quad (D1)$$

which are invariant under time-reversal and the D_{4h} symmetry group. Here $c_{\mathbf{k}\mu\alpha}^\dagger$ creates an electron with crystal momentum \mathbf{k} in the orbital $\mu \in \{d_{xz}, d_{yz}, p_z\}$ with spin α and $i = 0..4$. For simplicity, we henceforth use the notation, $c_{\mathbf{k}d_{xz}}^\dagger \equiv d_{xz}^\dagger$, etc. Since we are interested in a minimal description of the physics in the vicinity of Γ -Z, we consider terms upto quadratic order in k_x and k_y and upto nearest neighbor hopping along z . The symmetry constrained Hamiltonian takes the form $H = \sum_{\mathbf{k}} \Psi_{\mathbf{k}}^\dagger \tilde{h}_{\mathbf{k}} \Psi_{\mathbf{k}}$ with $\Psi_{\mathbf{k}} = (p_z, d_{yz}, d_{xz})^T$ and the Hermitian

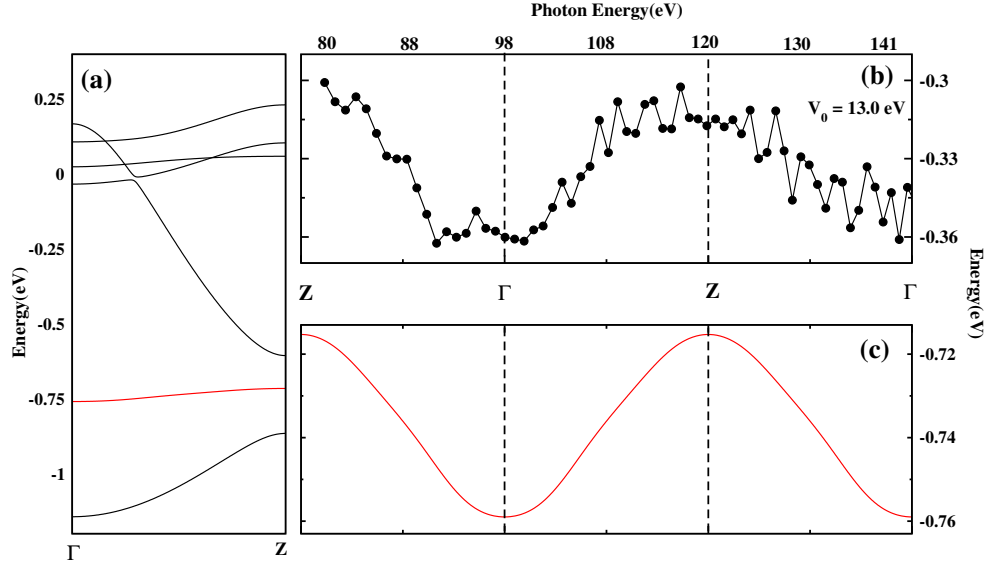


FIG. 6. (a) Band structure of FeSeTe along Γ -Z direction calculated from the DFT. (b) Experimental band of FeSeTe with respect to photon energy (upper x-axis) and $k_z/(\pi/c)$ (lower x-axis) observed in ARPES measurements. Here, π/c is reciprocal lattice vector corresponding to the lattice parameter c of FeSeTe. The experimental band exhibits a high qualitative resemblance to the DFT band in Fig. 6(a) marked with red colour. This calculated band is plotted separately an extended Brillouin zone in (d). In Fig. 6(b) inner potential $V_0 = 13.0$ eV is used to convert the photon energies dependency of the experimental band to corresponding k_z dispersion.

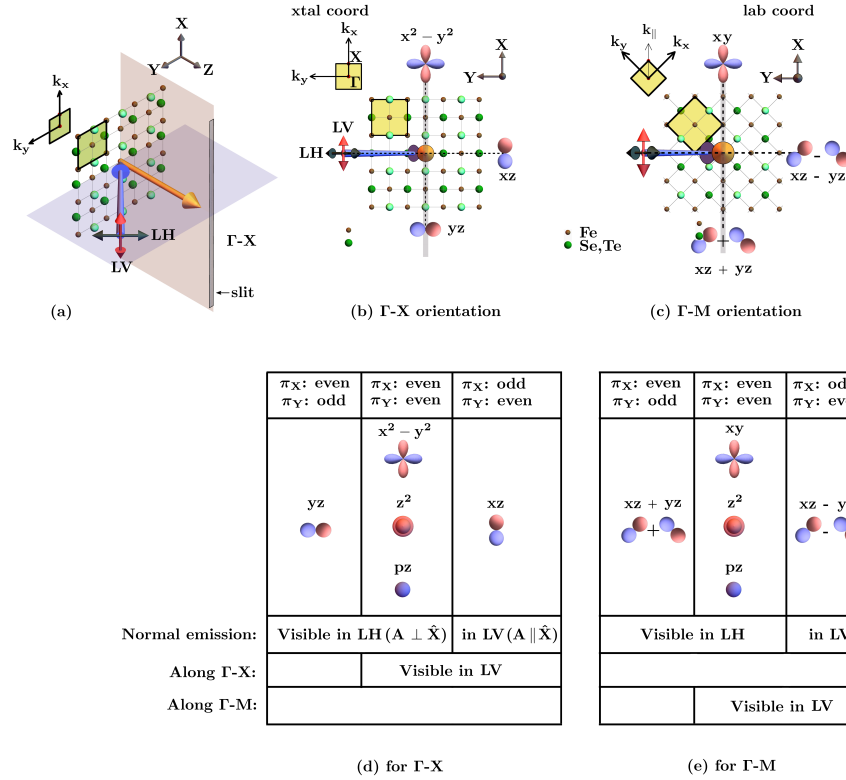


FIG. 7. (a) Schematic view of s-type ARPES set-up, with incident plane (blue) horizontal (YZ), and emission plane (orange) vertical (XZ). We use (X, Y, Z) to denote lab frame coordinates and (x, y, z) for sample coordinates consistent with the crystal axes. (b,c): Views along Z-axis of the sample oriented with analyzer slit along Γ -X (in panel (b)) and oriented along Γ -M (in panel (b)). We also show orbitals that are eigenstates of reflection in the incident and emission planes. (d and e): ARPES selection rules corresponding to panels (b) and (c) respectively; see text for details.

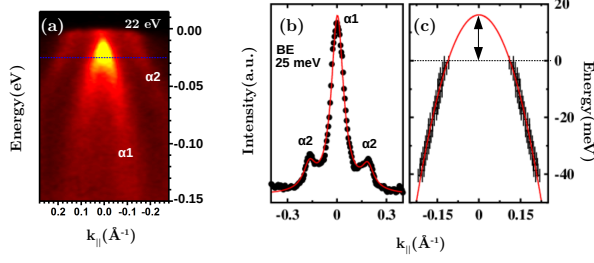


FIG. 8. (a) ARPES image of sample FeSeTe oriented along the Γ -M direction at photon energy of 22 eV using LH polarization and at temperature ~ 6 K. (b) MDC cut at BE = 25 meV (blue dotted line) from the ARPES image (a), where red curve is Lorentzian function fitted to this MDC data. (c) Band dispersion of $\alpha 2$ band obtained from the MDC peak fitting(b) and its top($\epsilon_{\alpha 2}$) is estimated from the parabolic fitting(red).

matrix

$$\tilde{h}_{\mathbf{k}} = \begin{pmatrix} \epsilon_p & f_y(\mathbf{k}) & f_x(\mathbf{k}) \\ \cdot & \epsilon_d + (k_x^2 - k_y^2)C_1 & f_{xy}(\mathbf{k}) \\ \cdot & \cdot & \epsilon_d - (k_x^2 - k_y^2)C_1 \end{pmatrix}$$

with

$$\begin{aligned} f_x(\mathbf{k}) &= [S_0 + (k_x^2 + k_y^2)S_1 + (k_x^2 - k_y^2)S_2] \sigma_y + k_x k_y \sigma_x S_3 \\ &\quad + i k_x C_2 - k_y \sigma_z C_3 \\ f_y(\mathbf{k}) &= -[S_0 + (k_x^2 + k_y^2)S_1 - (k_x^2 - k_y^2)S_2] \sigma_x - k_x k_y \sigma_y S_3 \\ &\quad + i k_y C_2 + k_x \sigma_z C_3 \\ f_{xy}(\mathbf{k}) &= k_x k_y C_4 + i \sigma_z \epsilon_{\text{SOC}} + i(k_{\parallel} \cdot \sigma_{\parallel}) S_4 \end{aligned} \quad (\text{D2})$$

where $\epsilon_{\mu} = \epsilon_{\mu}^0 + k_{\parallel}^2/2m_{\mu} + t_{z\mu} \cos k_z + t_{\text{diag}\mu} k_{\parallel}^2 \cos k_z$, $C_i = t_{i0} + t_{iz} \cos k_z$ and $S_i = t_i' \sin k_z$ are even and odd functions of k_z , k_{\parallel} and σ_{\parallel} are the in-plane projections of \mathbf{k} and σ , all coefficients are real and all momenta are rescaled by the appropriate lattice constants $k_x \rightarrow k_x a$, $k_y \rightarrow k_y a$, $k_z \rightarrow k_z c$. In the following, we step through the derivation of this Hamiltonian by enumerating the eigenstates of the D_{4h} point group symmetries.

D_{4h} is generated by C_4 , π_x (reflections in the YZ plane) and inversion. Under C_4 , $d_{xz} \rightarrow d_{yz}$, $d_{yz} \rightarrow -d_{xz}$, and we list below their Hermitian bilinears that are eigenstates of C_4 . Clearly,

	C_4	π_x
$d_{xz}^{\dagger} d_{xz} + d_{yz}^{\dagger} d_{yz}$	1	1
$d_{xz}^{\dagger} d_{xz} - d_{yz}^{\dagger} d_{yz}$	-1	1
$d_{xz}^{\dagger} d_{yz} + d_{yz}^{\dagger} d_{xz}$	-1	-1
$i d_{xz}^{\dagger} d_{yz} - i d_{yz}^{\dagger} d_{xz}$	1	-1

$d_{xz}^{\dagger} d_{xz} + d_{yz}^{\dagger} d_{yz}$ is invariant under the point group symmetries, and $i(d_{xz}^{\dagger} d_{yz} - d_{yz}^{\dagger} d_{xz})$ transforms like σ_z . The most general on-site Hamiltonian is therefore

$$h_{\mathbf{k}0} = \epsilon_p^0 p_z^{\dagger} p_z + \epsilon_d^0 (d_{xz}^{\dagger} d_{xz} + d_{yz}^{\dagger} d_{yz}) + i \sigma_z \lambda_1 (d_{xz}^{\dagger} d_{yz} - d_{yz}^{\dagger} d_{xz}) \quad (\text{D3})$$

where the coefficients are required to be real because of time-reversal invariance.

Next we consider nearest neighbor hopping along z . The availability of an inversion-odd form factor allows the possibility of hybridization between p_z and an appropriate combination of d orbitals that is invariant under C_4 and π_x . Such a combination results from mixing with the in-plane spin operators which also transform into each other under C_4 . The

	C_4	π_x
$\sigma_x d_{yz} - \sigma_y d_{xz}$	1	1
$\sigma_x d_{yz} + \sigma_y d_{xz}$	-1	1
$\sigma_x d_{xz} - \sigma_y d_{yz}$	-1	-1
$\sigma_x d_{xz} + \sigma_y d_{yz}$	1	-1

Hamiltonian along $\Gamma - Z$ thus has the following extra terms with the out-of-plane momentum $k_z \rightarrow k_z c$ rescaled by the c -axis lattice constant c

$$\begin{aligned} h_{\mathbf{k}z} &= 2 \cos k_z [t_{zp}^0 p_z^{\dagger} p_z + t_{zd}^0 (d_{xz}^{\dagger} d_{xz} + d_{yz}^{\dagger} d_{yz}) + \\ &\quad i \sigma_z \lambda_2 (d_{xz}^{\dagger} d_{yz} - d_{yz}^{\dagger} d_{xz})] \\ &\quad - 2 \sin k_z \lambda_3 [p_z^{\dagger} (\sigma_x d_{yz} - \sigma_y d_{xz}) + \text{h.c.}] \end{aligned} \quad (\text{D4})$$

where time-reversal invariance again requires the coefficients to be real. This leads to the model in Eq. (1).

The in-plane dispersion in the vicinity of ΓZ can be modelled by $\mathbf{k} \cdot \mathbf{p}$ perturbation theory, neglecting terms cubic or higher order in k_{\parallel} . At quadratic order, the C_4 -odd form factors $k_x^2 - k_y^2$ and $k_x k_y$ result in the following terms

$$\begin{aligned} h_{\mathbf{k}\parallel,1} &= \left(\frac{k_x^2 - k_y^2}{2m'} \right) (d_{xz}^{\dagger} d_{xz} - d_{yz}^{\dagger} d_{yz}) + \frac{k_x k_y}{2m''} (d_{xz}^{\dagger} d_{yz} + d_{yz}^{\dagger} d_{xz}) \\ &\quad + \left(\frac{k_x^2 - k_y^2}{2m_{\text{SOC},1}} \right) p_z^{\dagger} (\sigma_x d_{yz} + \sigma_y d_{xz}) + \frac{k_x k_y}{2m_{\text{SOC},2}} p_z^{\dagger} (\sigma_x d_{xz} - \sigma_y d_{yz}) \end{aligned} \quad (\text{D5})$$

in addition to those derived from each of the invariants in Eqs. (D3),(D4) by multiplying the C_4 invariant form factor $k_x^2 + k_y^2$ and in Eq. (D5) by multiplying the inversion-even form factor $\cos k_z$. Here and henceforth, k_{\parallel} is rescaled by the in-plane lattice constant a : $k_{x,y} \rightarrow k_{x,y} a$ and $\hbar = 1$.

In addition, there are linear terms in k_{\parallel} combined with σ_{\parallel} into the following C_4 eigenstates. This results in only one

	C_4	π_x
$\sigma_x k_y - \sigma_y k_x$	1	1
$\sigma_x k_y + \sigma_y k_x$	-1	1
$\sigma_x k_x - \sigma_y k_y$	-1	-1
$\sigma_x k_x + \sigma_y k_y$	1	-1

additional term in the Hamiltonian

$$h_{\mathbf{k},\times} = -i v_{\times} \sin k_z (\sigma_x k_x + \sigma_y k_y) (d_{xz}^{\dagger} d_{yz} - d_{yz}^{\dagger} d_{xz}) \quad (\text{D6})$$

the other three similar terms being inadmissible since hermiticity requires their coefficients to be real and time-reversal invariance requires them to be imaginary.

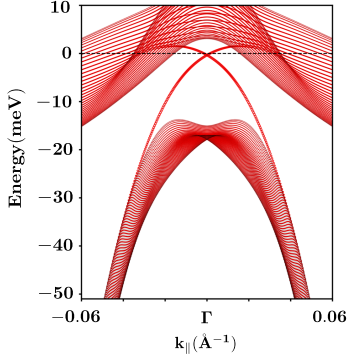


FIG. 9. Dirac surface state as seen in the calculated bandstructure of a 40-layer slab. Marker size is indicative of the weight on the top layer. Here, $\epsilon_p^0 = 29$, $\epsilon_d^0 = 1$, $t_{zp} = 22$, $t_{zd} = -5$, $\lambda_1 = 8$, $\lambda_3 = 8$, $1/m_p = 3000$, $1/m_d = -1500$, $1/m'' = -5700$, $v_{pd0} = 82$ (in meV) and all other parameters are set to 0.

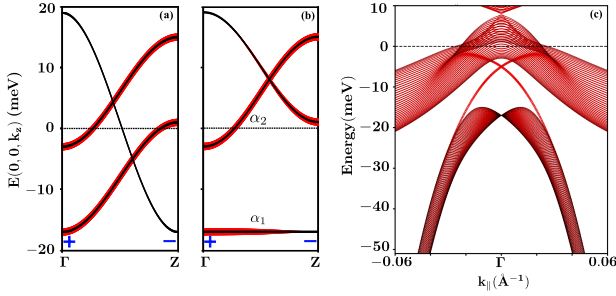


FIG. 10. Model calculations for a different choice of parameters, showing (a) dispersion along ΓZ without d - p mixing $\epsilon_p^0 = 1$, $\epsilon_d^0 = -1$, $t_{zp} = 9$, $t_{zd} = -4.5$, $\lambda_1 = 7$, (in meV) (b) with p - d mixing turned on, $\lambda_3 = 4.5$, (c) surface bandstructure of 40-layer slab with $1/m_p = 3000$, $1/m_d = -1500$, $1/m'' = -5700$, $v_{pd0} = 82$ as before.

Lastly, away from ΓZ , k_{\parallel} combines with d -orbitals to allow additional p - d coupling terms of the form

$$\begin{aligned} h_{\mathbf{k},pd} = & (v_{pd0} + 2v_{pdz} \cos k_z) p_z^{\dagger} (k_x d_{xz} + k_y d_{yz}) + \text{h.c.} \\ & + (v'_{pd0} + 2v'_{pdz} \cos k_z) \sigma_z p_z^{\dagger} (k_x d_{yz} - k_y d_{xz}) + \text{h.c.} \end{aligned} \quad (\text{D7})$$

This leads to the most general $\mathbf{k} \cdot \mathbf{p}$ Hamiltonian consistent

with the point group and time-reversal symmetries, which has the form shown in Eq. (D2).

Appendix E: Calculation of surface band structure

The band inversion along ΓZ leads to a protected Dirac cone in the bandstructure of the (001) surface. To see this, we must consider a model in a slab geometry with translation symmetry broken along z . For simplicity, we consider the Hamiltonian $H = \sum_{\mathbf{k}} \Psi_{\mathbf{k}}^{\dagger} \tilde{h}_{\mathbf{k}} \Psi_{\mathbf{k}}$ along the ΓM direction where $\mathbf{k} = (k/\sqrt{2}, k/\sqrt{2}, k_z)$ with

$$\tilde{h}_{\mathbf{k}} = h_{\mathbf{k}} + \begin{pmatrix} \frac{k^2}{2m_p} & i v_{pd0} \frac{k}{\sqrt{2}} & i v_{pd0} \frac{k}{\sqrt{2}} \\ \cdot & \frac{k^2}{2m_d} & \frac{k^2}{4m''} \\ \cdot & \cdot & \frac{k^2}{2m_d} \end{pmatrix} \quad (\text{E1})$$

where $\Psi_{\mathbf{k}} = (c_{p_z}, c_{d_{yz}}, c_{d_{xz}})^T$ and $h_{\mathbf{k}}$ which describes the physics along ΓZ is given by Eq. (1). Substituting

$$\begin{aligned} & \sum_{k_z} 2 \cos k_z c_{\mathbf{k}\mu\sigma}^{\dagger} c_{\mathbf{k}\mu'\sigma'} \\ & \rightarrow \sum_{n_z} \left[c_{\mathbf{k}_{\parallel}\mu\sigma}^{\dagger}(n_z) c_{\mathbf{k}_{\parallel}\mu'\sigma'}(n_z + 1) + \text{h.c.} \right] \\ & \sum_{k_z} 2 \sin k_z c_{\mathbf{k}\mu\sigma}^{\dagger} c_{\mathbf{k}\mu'\sigma'} \\ & \rightarrow \sum_{n_z} \left[i c_{\mathbf{k}_{\parallel}\mu\sigma}^{\dagger}(n_z) c_{\mathbf{k}_{\parallel}\mu'\sigma'}(n_z + 1) + \text{h.c.} \right] \end{aligned} \quad (\text{E2})$$

captures the breaking of translation symmetry at the surface, where $c_{\mathbf{k}\mu\sigma}^{\dagger}(n_z)$ creates an electron in orbital μ with spin σ on the layer n_z with in-plane momentum \mathbf{k}_{\parallel} . The resulting surface bandstructure with the Dirac cone is shown in Fig. 9.

We note that unlike the k_z dispersion presented in the main text, the model parameters controlling the in-plane dispersion are not constrained by the experimental data. From the many symmetry-allowed terms (see above) in the in-plane Hamiltonian, we have chosen to retain a minimal set of non-zero parameters that captures the α_1 dispersion and the surface Dirac cone. However, the presence of the surface Dirac cone is quite generic, independent of the precise values of the model parameters, as we show in Fig. 10 for a slightly different choice of parameters.

[1] Stefan Hufner, Photoelectron Spectroscopy: Principles and Applications, Springer, (1996).
 [2] Wang, P.-X. et al. Orbital characters determined from Fermi surface intensity patterns using angle-resolved photoemission spectroscopy *Phys. Rev. B* **85**, 214518 (2012).
 [3] Luttinger, J.M. Quantum Theory of Cyclotron Resonance in Semiconductors: General Theory J. M. Luttinger, *Phys. Rev.* **102**, 1030 (1956).
 [4] Inui, T., Tanabe, Y., and Onodera, Y. Group theory and its applications in physics **78** 367, Springer Science and Business Media

(2012).
 [5] Johnson, P. et al. Spin-Orbit Interactions and the Nematicity Observed in the Fe-Based Superconductors. *Phys. Rev. Lett.* **114**, 167001 (2015).
 [6] Chen, F. et al. Electronic structure of $\text{Fe}_{1.04}\text{Te}_{0.66}\text{Se}_{0.34}$ *Phys. Rev. B* **81**, 014526 (2010).
 [7] Okazaki, K. et al. Superconductivity in an electron band just above the Fermi level: possible route to BCS-BEC superconductivity. *Sci. Rep.* **4**, 4109 (2015).
 [8] Miao, H. et al. Isotropic superconducting gaps with enhanced

- pairing on electron Fermi surfaces in $\text{FeTe}_{0.55}\text{Se}_{0.45}$. *Phys. Rev. B* **85**, 094506 (2012).
- [9] Wang, Z. et al. Topological nature of the $\text{FeSe}_{0.5}\text{Te}_{0.5}$ superconductor *Phys. Rev. B* **92**, 115119 (2015).
- [10] Zhang, P. Observation of topological superconductivity on the surface of an iron-based superconductor *Science* **360**, 182-186 (2018).
- [11] Zhang, P. Multiple topological states in iron-based superconductors *Nat. Phys.* **15**, 41-47 (2019).
- [12] Watson, M. D. et al. Emergence of the nematic electronic state in FeSe . *Phys. Rev. B* **91**, 155106 (2015).
- [13] Hermanson, J. Final-state symmetry and polarization effects in angle-resolved photoemission spectroscopy *Sol. Stat. Comm.* **22**, 9 (1977).
- [14] Maletz, J. et al. Unusual band renormalization in the simplest iron-based superconductor FeSe_{1-x} . *Phys. Rev. B* **89**, 220506(R) (2014).
- [15] Xu, G., Lian, B., Tang, P., Qi, X.-L. and Zhang, S.-C. Topological Superconductivity on the Surface of Fe-Based Superconductors. *Phys. Rev. Lett.* **117**, 047001 (2016).
- [16] Cvetkovic, J and Vafeek, O. Space group symmetry, spin-orbit coupling, and the low-energy effective Hamiltonian for iron-based superconductors *Phys. Rev. B* **88**, 134510 (2013).